

Laser-based Powder Bed Fusion of Ti-6Al-4V Powder modified with SiO₂ Nanoparticles

Nicole Emminghaus (✉ n.emminghaus@lzh.de)

Laser Zentrum Hannover e.V. <https://orcid.org/0000-0002-9851-0820>

Robert Bernhard

Jörg Hermsdorf

Stefan Kaierle

Research Article

Keywords: additive manufacturing, laser-based powder bed fusion, Ti-6Al-4V, design of experiments, powder modification

Posted Date: April 15th, 2022

DOI: <https://doi.org/10.21203/rs.3.rs-1545400/v1>

License:   This work is licensed under a Creative Commons Attribution 4.0 International License.

[Read Full License](#)

Laser-based Powder Bed Fusion of Ti-6Al-4V Powder modified with SiO₂ Nanoparticles

Nicole Emminghaus^{1*} · Robert Bernhard¹ · Jörg Hermsdorf¹ · Stefan Kaierle^{1,2}

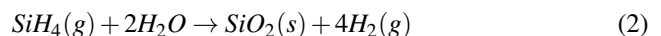
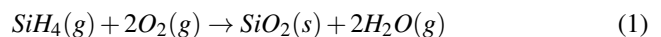
Received: date / Accepted: date

Abstract In laser-based powder bed fusion of metals (PBF-LB/M) residual oxygen in the processing atmosphere is regarded as disruptive and disadvantageous for the manufacturing process and the resulting component properties. A novel approach to eliminate residual oxygen is to add small amounts of silane to the argon process gas. Silane eliminates residual oxygen and forms SiO₂ nanoparticles, which in turn can be incorporated into the powder during the process. It is therefore necessary to evaluate the influence of these nanoparticles admixed to the metal powder. In this work, Ti-6Al-4V powder was modified with pyrogenic SiO₂ nanoparticles generated by the reaction of a silane argon gas mixture with ambient air. Modified and unmodified powder was analyzed and processed using statistically designed experiments. An increase of flow rate according to DIN EN ISO 4490 (from 33.3 to 32.5 s/50 g) and increase of apparent density according to DIN EN ISO 3923 (from 2.52 to 2.58 g/cm³) could be observed after powder modification. No statistically significant effects of the modification on roughness, porosity and hardness were found. The results demonstrate that powder modification using silane can lead to enhanced flowability without affecting the PBF-LB processing window of Ti-6Al-4V.

Keywords additive manufacturing · laser-based powder bed fusion · Ti-6Al-4V · design of experiments · powder modification

1 Introduction

In many different manufacturing processes, such as grinding, thermal spraying, dry machining or additive manufacturing (AM), the presence of oxygen in the processing atmosphere is a detrimental and thus undesired factor ([1–4]. An innovative approach to eliminate residual oxygen is the application of silane-doped process gases. This approach is currently investigated in the collaborative research center “Oxygen-free production”. Silane, also called silicon tetrahydride (SiH₄), is a metastable gas that reacts with oxygen and moisture even at room temperature and ambient air pressure. As it can be seen in Eq. 1, the reactants of the reaction are oxygen and silane while pyrogenic, amorphous silicon dioxide (also known as fumed silica) and water are the products of the first reaction. In a second reaction (Eq. 2) the water in turn or already existent moisture in the process atmosphere also reacts with silane and forms silicon dioxide and hydrogen [5, 6].



The resulting oxygen partial pressure can reach values of $\leq 10\text{-}20$ mbar [6]. Hence, it can be regarded as adequate to extreme high vacuum (XHV), which starts at 10^{-12} mbar [7]. The special feature of this approach, however, is that the conditions are achieved at normal pressure, which makes expensive vacuum equipment unnecessary. Especially for highly reactive metals like titanium, this approach promises

✉ N. Emminghaus
n.emminghaus@lzh.de
<https://orcid.org/0000-0002-9851-0820>

¹ Laser Zentrum Hannover e.V. (LZH)
Hollerithallee 8
D-30419 Hannover, Germany

² Leibniz Universität Hannover, Institut für Transport- und Automatisierungstechnik (ITA)
An der Universität 2
D-30823 Garbsen, Germany

the processing without disruptive oxide layers that normally form immediately when the surface is exposed to atmospheric oxygen. Titanium alloys are one of the most investigated metal materials in additive manufacturing, especially in the laser-based powder bed fusion process (PBF-LB). This processing technology enables the fabrication of highly complex geometries with internal or cellular structures and the economical production of individualized components. It is therefore predestined for the application in medical technology or the manufacturing of topology optimized lightweight components for the aerospace industry [8–10]. The PBF-LB/M processing window for Ti-6Al-4V, the most widely used titanium alloy, has been extensively researched and optimized toward low porosity and surface roughness in the last years [11–15]. Nevertheless, the reproducibility and component quality is limited by internal defects like gas pores or lack of fusion defects as well as oxidation processes that lead to decreased ductility and fatigue strength [16–18]. The application of a silane-doped argon atmosphere in PBF-LB is therefore promising. It could enable higher part qualities and increased reproducibility. The downside of this approach is the formation of SiO₂ dust, which is assumed to mix with the powder to be processed. It is not yet known how the formed SiO₂ particles affect the processability and component properties. From a different point of view, the inclusion of SiO₂ particles in the Ti-6Al-4V powder represents not only a contamination but can also be seen as a powder modification. SiO₂ nanoparticles already have a wide range of industrially relevant applications, the most relevant regarding this work is the application as a flow enhancing additive [19]. A well-known industrial product is Aerosil® from Evonik. Multiple applications for the modification of polymeric and metal powders have been reported, e.g. [20–22]. However, the explicit use for metal additive manufacturing has rarely been described in the literature so far. To improve the mixing and in situ-alloying of Al-Cu powder mixtures, Karg et al. modified the powder mixture with SiO₂ nanoparticles. The stabilization against segregation for small particles < 20 μm led to high homogeneity of the chemical elements in the processed specimens that was also supported by tensile tests [23]. In another work, Karg et al. used drycoating with SiO₂ nanoparticles to improve the flowability, measured by the static angle of repose, and layer deposition of Al-Si powder. High relative density of up to 99.97 % and a significant improvement in comparison to uncoated powder containing fine particles < 20 μm was demonstrated [24]. However, potential influences on microstructure and mechanical properties were not addressed in this work. Peng et al. also describes the idea of using nanoparticle dry coating with SiO₂ to improve the layer spreading of Ni-based metal powders [25]. Gaertner et al. dry coated equimolar alloy metal powder (CoCrFeNi) with SiO₂ nanoparticles to improve its flowability. They observed a reduction of the dynamic angle of repose by 50 %

and an increase of the bulk powder density by 30 % [26]. Nevertheless, as the powder was not subsequently processed, it is not known how this modification affects the process and part properties. Insufficient flowability represents a major limitation in the AM of some materials, especially fine powders. Consequently, by flow improvement by means of powder modification the range of processable materials could be expanded. At this time, the range of metal powders modified with SiO₂ nanoparticles is strongly limited and does not include studies on Ti-6Al-4V. It is therefore unknown how this modification affects the powder flow behavior and the subsequent PBF-LB process. The SiO₂ formation under XHV-adequate atmosphere cannot be prevented. It is important to know how this reaction product could influence the process and if the processing window needs to be adjusted to achieve maximum part quality. This work therefore aims to investigate the processing window for modified Ti-6Al-4V powder and to compare it to the one of unmodified powder regarding the roughness, porosity and hardness. For this purpose, the design of experiments approach is applied and a regression model is set up. In the following, we describe the applied materials and methods as well as the obtained results. Finally, a discussion and a conclusion are given.

2 Materials and Methods

The methodology can be divided into six substeps: powder modification consisting of SiO₂ generation and powder mixing, powder characterization, experimental planning according to the DoE (Design of Experiments) approach and the conduction of build jobs as well as specimen characterization as the final step. Fig. 1 shows the schematic workflow that was applied in this work. The single steps are described in detail in the following sections.

2.1 Powder Modification and Analysis

The powder material applied in this work was recycled gas atomized Ti-6Al-4V powder (grade 23) supplied by Heraeus Additive Manufacturing GmbH. The virgin powder has a specified particle size of 15-53 μm with a size distribution of D10 = 22 μm, D50 = 38 μm and D90 = 54 μm according to the manufacturer's datasheet. For the applied recycled powder, the size distribution is more narrow and the mean particle size is slightly higher than for virgin powder [27]. Recycling in this case means that the powder was reused multiple times and sieved with a mesh size of 63 μm after each process. For modification of the powder, a glass container with powder was placed inside a small glovebox (side length of 30 cm) filled with air. In a subsequent step, a gas mixture of argon 5.0 doped with 1 vol% silane was flowed into the

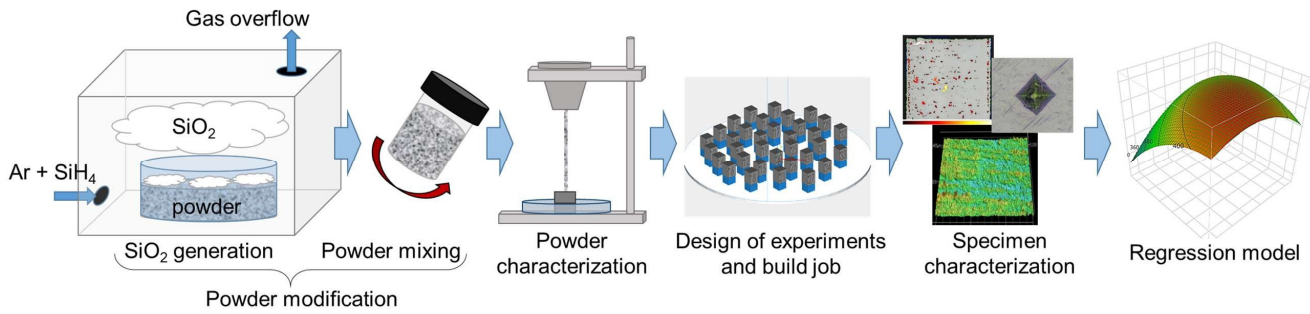


Fig. 1 Schematic representation of the applied workflow.

glovebox where it reacted with the ambient atmosphere according to Eq. 1 and 2. During the reaction in the glovebox, no stirring of the powder was applied. After deposition of the SiO₂ dust on the powder, the glass container was removed and the powder was manually mixed in a closed container to achieve a homogeneous distribution of the nanoparticles within the powder. The described procedure was chosen instead of admixing commercially available SiO₂ nanoparticles (e.g. Aerosil®) with the intention to simulate the powder contamination in the PBF-LB/M process conducted under this silane-doped atmosphere. In this way, it can be ensured that the nanoparticles went through the same formation process and have the same properties. The powder morphology and the homogeneous nanoparticle distribution as well as the nanoparticles themselves were analyzed using scanning electron microscopy (SEM, Quanta 400 FEG, FEI Company) and energy-dispersive X-ray spectroscopy (EDX). The EDX analysis was done with the software EDAX Genesis by AMETEK GmbH. Three SEM pictures of different modified powder particles were further analyzed by image processing with the open source software Fiji based on ImageJ to estimate the surface coverage of the nanoparticles. For this purpose, first the edge detection was applied to recognize the single nanoparticles. Then the image was transformed into a binary image, open contours were closed and subsequently the contours were filled. The processed images were then analyzed using the particle analysis function that calculates the ratio between the white (nanoparticles) and the black areas (underlying host particle surface) which corresponds to the surface coverage. Before additive processing, the flow rate and apparent density were analyzed in accordance with DIN EN ISO 3923 and 4490 using a Hall funnel.

2.2 Experimental Design and Equipment

To detect possible influences and interaction effects of the powder modification on the processing window, it is necessary to not only compare specimens made of modified and unmodified powder but to conduct a parameter study for

both types of powder. This way it is possible to detect shifts for optimum parameter combinations regarding the response variables roughness, porosity and hardness. An efficient way to minimize the required specimen size while maximizing the obtainable information is the DoE approach. It also enables the description of quantitative relationships, effect sizes and interactions between the factors (independent variables) and responses (dependent variables) by the derivation of a mathematical model in the form of regression polynomials. In this study, a rotatable central composite design (CCD) with an axial value of $\alpha = 1.682$ was chosen as it allows the evaluation of linear, quadratic and cubic effects as well as two-way interactions. The process parameters laser power P , scanning speed v and hatch distance h were varied on 5 levels each. The implemented factor levels are given in Table 1 and were chosen based on literature, the authors' experience and the machine limitations. All parameter combinations given by the chosen design were repeated twice in one build job except the central point, which was repeated 6 times to reduce prediction variance. This led to a total number of 34 specimens per build job. To achieve orthogonality of the experimental design and thus further improve accuracy of prediction, 9 replications of the central point would be necessary but due to limited space on the build platform, this was not feasible. For each type of powder, one build job with the described design was conducted. The build job design is shown in Fig. 2. The parameter combinations were assigned to the specimen IDs in a randomized manner and the specimens were oriented with a 45° angle with respect to the gas flow and recoating direction to minimize position dependent effects. Cubes with a side length of 5 mm on top of 3 mm wall support structures were chosen as specimen geometry. The contour was scanned after the infill but with the same parameters to reduce the number of influencing variables. An offset of 100 μm between infill and contour, a bidirectional scanning strategy with a rotation of 67° between adjacent layers and a constant layer thickness t of 30 μm were implemented. No platform heating was applied. An overview of all specimen IDs with the respective parameter settings can be found in the appendix (Table A1).

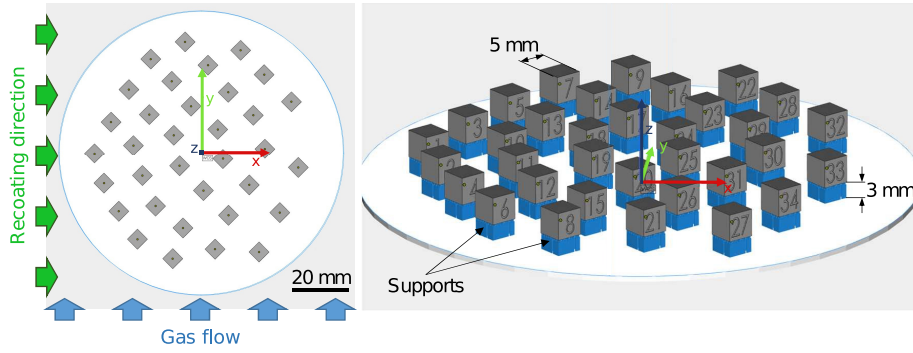


Fig. 2 Implemented build job layout with direction of gas flow, recoating movement and engraved specimen IDs.

Table 1 Levels of the varied processing parameters according to the central composite design.

Parameter	Levels				
Laser power (W)	115	145	175 ^c	205	235
Scanning speed (mm/s)	600	800	1000 ^c	1200	1400
Hatch spacing (μm)	40	60	80 ^c	100	120

^c center point parameter combination

The response values of interest in this study are porosity ϕ , top surface roughness S_{aTop} , side surface roughness S_{aSide} and hardness H . To evaluate the factor effects on these responses, a mathematical model was fitted using the least squares method. To reduce heteroscedasticity, all responses except the hardness where transformed using log-transformation. For the statistical analysis, a significance level of 5% (p-value > 0.05) was chosen. Effects with larger p-values were excluded from the model following the principle of strong effect heredity. This means that the effect can only be excluded when there is no significant dependent higher order effect left in the model. The generation of the experimental design as well as the statistical analysis of the experimental data was conducted using the statistics software JMP® (SAS Institute Inc.). The experiments were carried out on an industrial machine, TruPrint 1000 by Trumpf GmbH & Co. KG (Ditzingen, Germany), that is equipped with a 200 W ytterbium fiber laser (single mode, continuous wave, wavelength 1070 nm). It enables a minimum spot diameter of 30 μm that is created by a telecentric f-theta lens. A minimum residual oxygen content of 200 ppm was maintained using high purity argon as a process gas.

2.3 Specimen Characterization

The specimens were manually removed from the build platform and subsequently examined for their roughness by employing optical profilometry (OP). For all specimens, the side surface opposite to the engraved number and the top surface were analyzed using the confocal laser scanning microscope VK-X1000 series with a VK-X1100 measurement

unit (semiconductor laser with wavelength of 404 nm, height display resolution of 0.5 nm) by Keyence. The repeatability of the employed objective lens in combination with the laser confocal height measurement is 0.1 μm (1-sigma) and the accuracy is given by Eq. 3.

$$Accuracy = 1 + \frac{\text{measurement length } (\mu\text{m})}{100 \mu\text{m}} \quad (3)$$

The arithmetic mean roughness (S_a) based on a square area with a side length of 2 mm was used as the characteristic value for the roughness. S_a was chosen instead of its linear corollary R_a because different studies suggest that R_a is not sufficient to describe the surface topology of additively manufactured parts [28]. Selected specimens were further examined using SEM and EDX to investigate possible SiO_2 residuals on the surface. After surface characterization, all specimens were cold embedded in epoxy resin (Technovit Epox, Kulzer GmbH, Hanau, Germany), ground and polished (Tegramin, Struers ApS, Ballerup, Denmark). For every specimen, three cross-sections were made parallel to the build direction (BD) and analyzed with the light microscopy function of the VK-X1000 microscope. Using a python script developed at Laser Zentrum Hannover e.V. (LZH), the stitched microscopic images were first transformed to black and white with a given threshold value and in a subsequent calculation of the proportion of black and white pixels the porosity was determined. For the statistical evaluation, only the mean porosity of the three cross-sections per specimen was used. On the last cross-section of each specimen, the Vickers hardness HV0.1 was measured with an indentation time of 10 s (INNOVATEST NEXUS 4000 testing machine). Three indentations located halfway up the specimen, starting at 0.75 mm distance to the side surface and continuing towards the middle with a step size of 0.75 mm were conducted. Additionally the cross-sections were etched using Kroll's reagent and the microstructure was analyzed using light microscopy.

3 Results

3.1 Powder

Collected SiO₂ dust from the glovebox was analyzed regarding the nanoparticle size and chemical composition. Single nanoparticles show sizes ranging between 50 and 100 nm and are mainly forming larger agglomerates (Fig. 3 a). The EDX analysis confirms the composition of oxygen and silicon (Fig. 3 b).

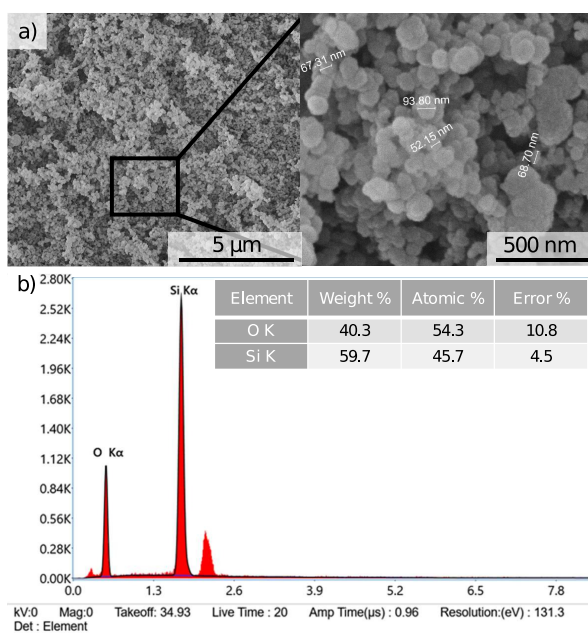


Fig. 3 SiO₂ dust collected from the glovebox: a) SEM images of the agglomerated nanoparticles with sizes between 50 and 100 nm; b) EDX analysis confirming the chemical composition of the SiO₂ nanoparticles.

Modified and unmodified powder were also analyzed using SEM. The SEM images (Fig. 4) show that the Ti-6Al-4V powder has a mainly spherical morphology with a smooth particle surface. Only few satellites were observed beneath the larger particles, what can be attributed to the coarsening effect of powder recycling [27]. Regarding the modified powder, a homogeneous distribution of the SiO₂ nanoparticles on the surface of the Ti-6Al-4V host particles was observed. The nanoparticles were evenly distributed on all powder particles. The image processing and analysis using Fiji revealed a surface coverage between 14 and 17 %. The flowrate was evaluated in accordance with DIN EN ISO 4490. For unmodified Ti-6Al-4V, a mean flow rate of 33.3 s/50 g was obtained while the modification with SiO₂ nanoparticles led to a mean flow rate of 32.5 s/50 g, an improvement by 3.4 %. Additionally, the apparent density was measured according to DIN EN ISO 3923. Here an increase from 2.51 g/cm³ for unmodified to 2.58 g/cm³ for modified powder, an increase

by 2.8 %, could be observed. The results of the flowability characterization are summarized in Table 2. The statistical analysis showed a significant influence of the powder modification on the flow rate ($p = 0.0139$) and on the apparent density ($p < 0.0001$). The r^2 -value for the regression of the flowrate ($r^2 = 0.81$) was smaller than the one for the apparent density ($r^2 = 0.99$), which can be explained by the different standard deviations (Table 2). However, the effect size of the powder on the flowrate was larger (0.40) compared to the effects size for the apparent density (-0.03).

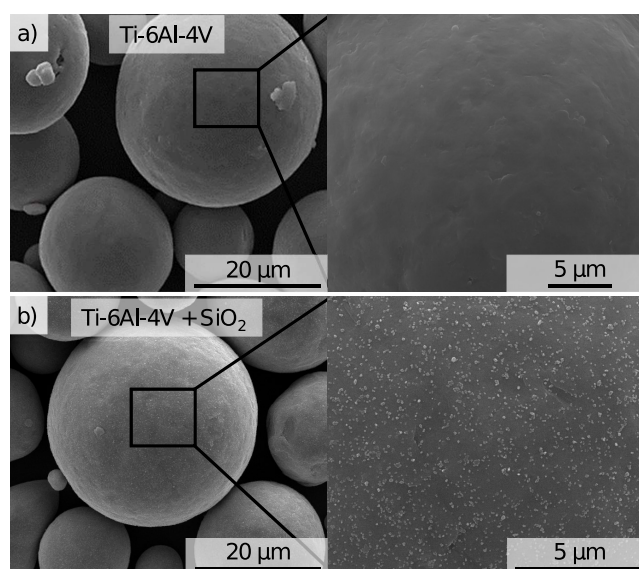


Fig. 4 SEM images of Ti-6Al-4V powder: a) unmodified powder, b) modified powder with SiO₂ nanoparticles.

3.2 Surface Characterization

The surface roughness was investigated on the top as well as on the side surface of the cube specimens. For the top surface roughness a maximum of 51.7 μm ($P = 130 \text{ W}$, $v = 1000 \text{ mm/s}$, $h = 60 \mu\text{m}$, unmodified powder) and a minimum of 7.8 μm ($P = 170.2 \text{ W}$, $v = 700 \text{ mm/s}$, $h = 80 \mu\text{m}$, modified powder) was observed. For the side surface roughness the maximum was 33.5 μm ($P = 145 \text{ W}$, $v = 195.5 \text{ mm/s}$, $h = 80 \mu\text{m}$, modified powder) and the minimum was 8.1 μm ($P = 145 \text{ W}$, $v = 700 \text{ mm/s}$, $h = 80 \mu\text{m}$, unmodified powder). A multiple linear regression and statistical analysis were conducted after log-transformation of the responses to reduce heteroscedasticity. Only laser power and scanning speed had a significant influence on top and side surface roughness (Table 3). No significant effect could be observed for the hatch distance and the powder modification. For both types of roughness, also quadratic and cubic as well as two-way interaction effects were found to be statistically significant.

Table 2 Results of standardized powder characterization according to DIN EN ISO 4490 and 3923.

Characteristic		Ti-6Al-4V	Ti-6Al-4V + SiO ₂
Flowrate (s/50 g)	Mean	33.3	32.5
	Standard deviation	0.2	0.3
Apparent density (g/cm ³) (wt%)	Mean	2.51	2.58
	Standard deviation	0.01	<0.01

The quadratic effect of scanning speed in the case of the top surface roughness and the linear effects of laser power and scanning speed in the case of the side surface roughness were left in the model although they have p-values of >0.05 . This is due to the principle of strong effect heredity explained in section 2.2. The contour plots visualize the evaluated processing map (Fig. 5). With increasing scanning speed and decreasing laser power the top surface roughness increases. For the side surface roughness a minimum can be achieved for medium laser power and scanning speed while the roughness increases with decreasing scanning speed. Due to high variance of the roughness values on both surfaces, the r^2 -values of the regression models were relatively low with $r^2 = 0.44$ for the top surface and $r^2 = 0.46$ for the side surface. The prediction expressions are given in the appendix.

Besides optical profilometry also SEM (Fig. 6) and EDX were used to characterize the as-built surface. On the side surface, sintered and partly melted particles were visible. The top surface showed the partly overlapping scan paths and some smaller particles that have their origin in spattering and the balling effect. The SEM images did not show any SiO₂ particles left on the as-built surface made of the modified powder (Fig. 6).

3.3 Porosity

Across all experiments, a minimum porosity of 0.03 % ($P = 160$ W, $v = 1000$ mm/s, $h = 60$ μ m, unmodified) and a maximum porosity of 5.30 % ($P = 130$ W, $v = 1000$ mm/s, $h = 100$ μ m, modified) were obtained. The quadratic effect of scanning speed had the strongest influence on the porosity followed by the interaction effect of laser power and scanning speed. The hatch distance also had a significant but smaller effect. The interactions between hatch distance and the two other varied process parameters were all significant (Table 4). No significant effect of the powder modification was observed. The contour plot (Fig. 7) shows the dependency of the porosity on the two most influential factors, scanning speed and laser power. A low porosity can be achieved for medium to high laser power at medium scanning speed of 700 mm/s. From this point on the porosity increases for increasing as well as decreasing scanning speed. The regression model has an r^2 -value of 0.69. The prediction expression can be found in the appendix.

3.4 Hardness

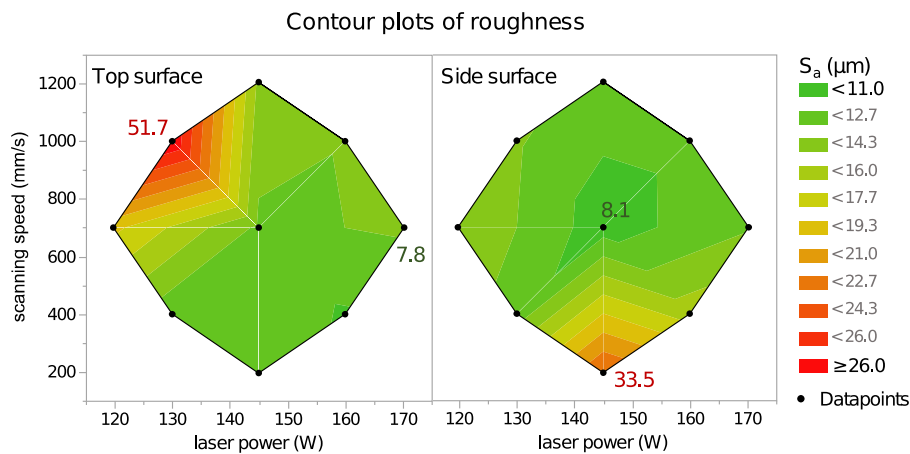
Regarding the hardness, a maximum of 445.7 HV0.1 ($P = 145$ W, $v = 195.5$ mm/s, $h = 80$ μ m, unmodified) and a minimum of 349.0 HV0.1 ($P = 130$ W, $v = 1000$ mm/s, $h = 100$ μ m, modified) were observed. The powder modification did not show a significant influence. The hardness was significantly influenced by the three process parameters scanning speed, laser power and hatch distance. Thereby, the scanning speed and the hatch distance showed the largest effect sizes and the lowest p-values (Table 5). With increasing hatch distance and scanning speed, the hardness decreases (Table 5, Fig. 8). For the laser power there is a setting for maximum hardness that depends on the setting of the scanning speed, as there is a significant interaction between these factors. For medium scanning speed of 700 mm/s, a maximum hardness can be obtained for a medium laser power of 145 W (Fig. 8). The goodness-of-fit for the regression model of hardness is $r^2 = 0.47$. The prediction expression based on the estimates is given in the appendix.

3.5 Microstructure

To investigate possible effects of the powder modification on the microstructure, etched cross-sections were analyzed. There were no noticeable differences between specimens made of unmodified and modified powder, as exemplarily shown for different applied volume energy densities in Fig. 9. In both cases, a fine microstructure with prior- β -grains oriented in build direction (BD) and α' -martensite needles oriented at 45° to the β -grains were observed (Fig. 9). With increasing energy input, a coarsening of the microstructure with larger prior- β -grains was observed. For parameter combinations that lead to massive overheating, as for $E_V = 309.1$ J/mm³ in Fig. 9, the prior- β -grains become less oriented. Additionally, the observed martensite needles are smaller. For each powder type, four selected cross-sections were also analyzed using EDX. No significant differences in silicon content could be detected (Appendix A2). Since the oxygen content measured for the cross-sections was below the minimum detection limit, no inferences on differences in oxygen content can be made.

Table 3 Parameter estimates of the regression model for the top and side surface roughness after log-transformation.

Term	Estimate	Std.-Error	t-Value	p-Value
Top surface				
Intercept	2.5741	0.0468	55.04	<0.0001
Scanning speed	0.3509	0.0843	4.16	<0.0001
Laser power · Scanning speed	-0.1601	0.0502	-3.19	0.0023
Laser power	-0.1561	0.0384	-4.06	0.0001
Scanning speed ²	-0.1127	0.0427	-2.64	0.0104
Scanning speed ³	0.0097	0.0394	0.25	0.8063
Side surface				
Intercept	2.2950	0.0479	47.94	<0.0001
Scanning speed ²	0.1623	0.0315	5.15	<0.0001
Laser power · Scanning speed	-0.0890	0.0392	-2.27	0.0264
Laser power ²	0.0820	0.0315	2.60	0.0116
Scanning speed ³	-0.0801	0.0332	-2.41	0.0190
Scanning speed	0.0369	0.0657	0.56	0.5758
Laser power	-0.0025	0.0299	-0.08	0.9351

**Fig. 5** Contour plot of the top and side surface roughness depending on the factors scanning speed and laser power. The colors indicate the roughness from small values (green) to high values (red). Maximum and minimum values are marked.

4 Discussion

This research focused on the effect of SiO₂ nanoparticle modification of Ti-6Al-4V powder on the PBF-LB process. Therefore, the powder was characterized in a standardized manner and subsequently, the response variables top and side surface roughness, porosity and hardness as well as the microstructure were evaluated. It was found that the powder modification leads to a reduced flow rate and thus a better flowability as well as an increased apparent density. On the other side, no significant effect of the powder modification on the processing window and part properties was observed. The improved flowability was also described in other works on powder modification, e.g. [23–26]. By covering the host particles surfaces, the nanoparticles on the one hand increase the apparent roughness and thus the distance between two particles. As a consequence the Van-der-Waals forces be-

tween the particles are reduced [26]. On the other hand, the nanoparticles act as a ball bearing between the larger host particles and therefore enhance flow [19]. Another aspect is the formation of liquid bridges which also plays an important role in cohesive behavior of powders [29]. Yang et al. for example attributed the observed improvement of flowability after modification with hydrophobized nanosilica to the reduction of liquid bridges [30]. Fig. 10 illustrates these mechanisms.

As stated by Gaertner et al., the concentration and size of the nanoparticles is an important criteria [26]. The amount of surface coverage of 14-17 % in this study is in the range of 10-20 % for which other studies achieved optimal fluidization [31–33]. While other types of nanoparticles like carbon black, Al₂O₃ or SiC used to modify powder for additive manufacturing led to significant changes in laser absorption [34, 35] or mechanical properties [36], the application of SiO₂ particles

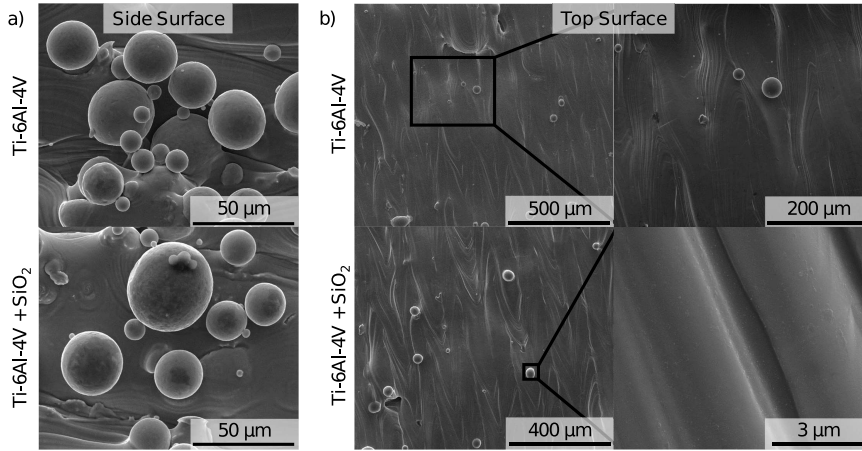


Fig. 6 SEM images of as-built surfaces for both types of powder: a) Side surface with sintered particles, b) top surface with visible scan tracks and without remaining SiO₂ particles on the surface.

Table 4 Parameter estimates of the regression model for porosity after log-transformation.

Term	Estimate	Std.-Error	t-Value	p-Value
Intercept	-1.8816	0.1604	-11.73	<0.0001
Scanning speed ²	0.7526	0.1055	7.14	<0.0001
Laser power · Scanning speed	-0.5827	0.1310	-4.45	<0.0001
Laser power	-0.5779	0.1003	-5.76	<0.0001
Scanning speed · Hatch distance	0.4149	0.1310	3.17	0.0024
Laser power ²	0.3276	0.1055	3.11	0.0029
Hatch distance	0.2867	0.1003	2.86	0.0059
Laser power · Hatch distance	0.2649	0.1310	2.02	0.0478
Scanning speed	-0.0849	0.1003	-0.85	0.4005

Table 5 Parameter estimates of the regression model for hardness.

Term	Estimate	Std.-Error	t-Value	p-Value
Intercept	414.0361	3.2323	128.09	<0.0001
Scanning speed	-8.3912	2.0218	-4.15	0.0001
Hatch distance	-8.2953	2.0218	-4.10	0.0001
Laser power · Scanning speed	5.3438	2.6416	2.02	0.0475
Laser power ²	-5.1552	2.1260	-2.42	0.0183
Laser power	5.0632	2.0218	2.50	0.0150
Scanning speed ²	-4.6102	2.1260	-2.17	0.0340

in this work did not show influences regarding these aspects. However, as powder in general has a higher laser absorption than bulk material due to multiple reflections in the powder bed [37], it is possible that small changes of the powder surface structure due to modification are not noticeable. Future research will therefore include absorption measurements using an integrating sphere. However, the process parameters laser power, scanning speed and hatch distance showed significant effects. These effects can partly be explained by taking the volume energy density E_V into account, given by Eq. 4.

$$E_V = \frac{P}{v \cdot h \cdot t} \quad (4)$$

Other works have shown a dependence of the roughness on the volume energy density [38–41] that can also be confirmed in this work. With decreasing scanning speed and increasing laser power, E_V also increases. This leads to larger melt pools and increased sintering of particles on the side surface [40, 42]. Consequently, the side surface roughness increases. With increasing scanning speed and decreasing

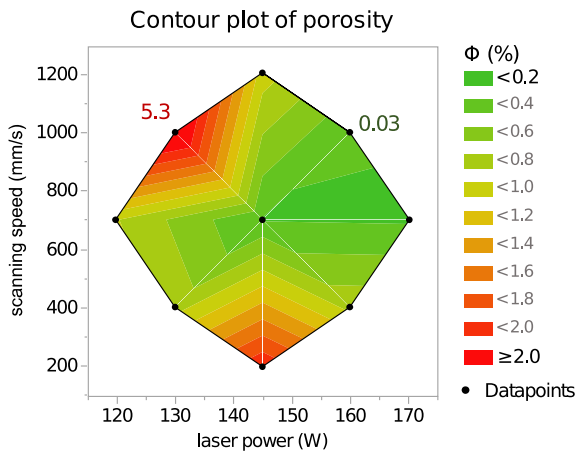


Fig. 7 Contour plot of the porosity depending on the factors scanning speed and laser power. The colors indicate the porosity from small values (green) to high values (red). Maximum and minimum values are marked.

laser power E_V decreases. Below a certain threshold, the energy introduced is no longer sufficient to melt the powder material completely. Due to insufficient melting and high melt viscosity, discontinuous melt tracks are generated and a high top surface roughness results [43]. This in turn is related to the formation of lack-of-fusion (LoF) defects that lead to increased porosity [44]. This correlation of porosity and roughness and the influence of the melting behavior was also shown by Wang et al. [39]. In our work, it was shown that a high porosity is obtained either for low (high scanning speed, low laser power) or high volume energy density (low scanning speed, high laser power). These two areas of high porosity correspond to different types of pores. While the mentioned LoF defects occur for low energy input [44], spherical gas pores, also known as keyhole pores, are generated when the energy input is too high so that overheating and evaporation take place [45, 46]. The interaction effect of laser power and scanning speed showed a strong and significant effect in all regression models. In contrast to the roughness models, the models for porosity and hardness additionally contained significant effects of the hatch distance. As with the scanning speed, the volume energy density is inversely proportional to the hatch distance (Eq. 4). A decreasing E_V due to increasing hatch distance results in insufficient melting of the powder and therefore increased porosity. Further, with increasing hatch distance and scanning speed, the hardness decreases. Regarding the laser power, the hardness can be reduced either for low or for high values. The hardness decrease for low volume energy density is likely to be attributed to the insufficient melting of the powder and the resulting LoF defects. Similar effects were also reported in the literature [47–50]. When the volume energy input is high enough to cause evaporation and keyhole pores, larger melt pools are

obtained resulting in slower solidification, grain coarsening and therefore a decrease in hardness. All presented regression models, except the one for porosity, showed a medium goodness-of-fit slightly below $r^2 = 0.5$. There is consequently a high proportion of variation in the experimental data that cannot be explained by the models. This is attributed to the high variance inherent to the PBF-LB process that is not fully understood and under control yet. There is a high number of influencing factors and it is not possible to include all of them in a regular study. Accordingly, the observed variance could be explained to irregularities in the gas flow, powder deposition or inhomogeneity of beam intensity across the build platform [51–53]. It is also important to mention that the models are only applicable in the investigated parameter range and transferability to other machine set-ups or other materials is limited. Besides the effects of the SiO₂ nanoparticles on the process, it is also of interest how the nanoparticles are affected during the PBF-LB process. Since no nanoparticles were found on the specimens' surfaces, it is assumed that they were partly incorporated into the melt and to another part evaporated during the process. A removal by the inert gas flow is rather unlikely. A sample of the unmelted powder was taken after the build-process finished and was analyzed using SEM. The particles were still covered by nanoparticles without a visible change in the amount or distribution. Although the carriage of smaller powder particles by the gas flow takes place during processing and is regarded as one reason for coarsening of recycled powder [54, 55], it is assumed that this is not the case for the nanoparticles adhering to the host particles surfaces. An indicator for melt incorporation would be a change in microstructure and mechanical properties as observed in other works [36, 56–58]. Silicon acts as a beta stabilizer and promotes grain refinement [59, 60]. When the solubility of silicon in titanium is exceeded, silicides are formed. The silicides improve the creep resistance but can also have negative effects on the mechanical properties [61]. Taking into account the high temperatures and cyclic reheating during the process, incorporated SiO₂ nanoparticles can react with the surrounding titanium matrix. The silicon then forms silicides with the titanium while the oxygen diffuses into the titanium matrix [62]. However, changes in microstructure, chemical composition or hardness could not be observed in this study. Nevertheless, it is possible that the used amount of nanoparticles was too small to lead to significant changes in microstructure and hardness. To evaluate this hypothesis further, further investigations, especially tensile tests and more detailed microstructure analysis, will be necessary. Since this work focused on the processing window and the parameter influences on porosity and roughness of the as built specimens, a thorough study of the microstructure and depending mechanical properties will be part of future studies. A limitation of this study is that there was no fixed mixing ratio of powder and nanoparticles. The

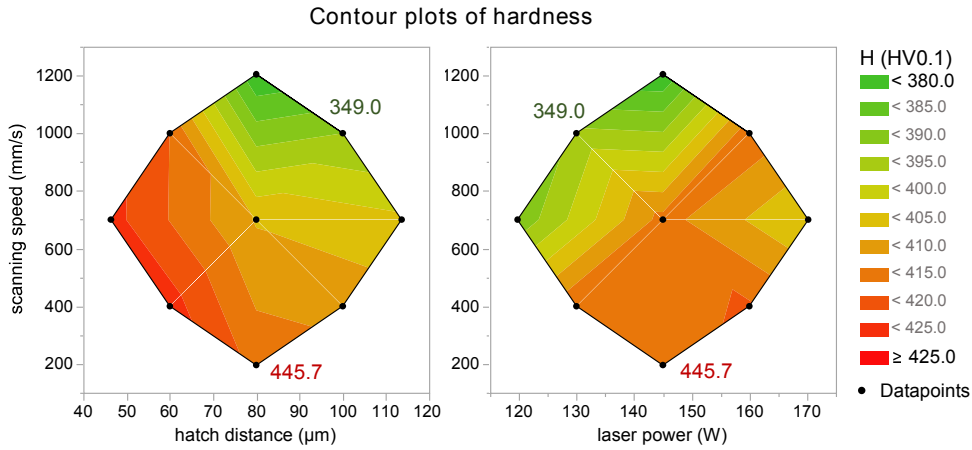


Fig. 8 Contour plot of the hardness depending on the factors scanning speed, hatch distance and laser power. The colors indicate the hardness from small values (green) to high values (red). Maximum and minimum values are marked.

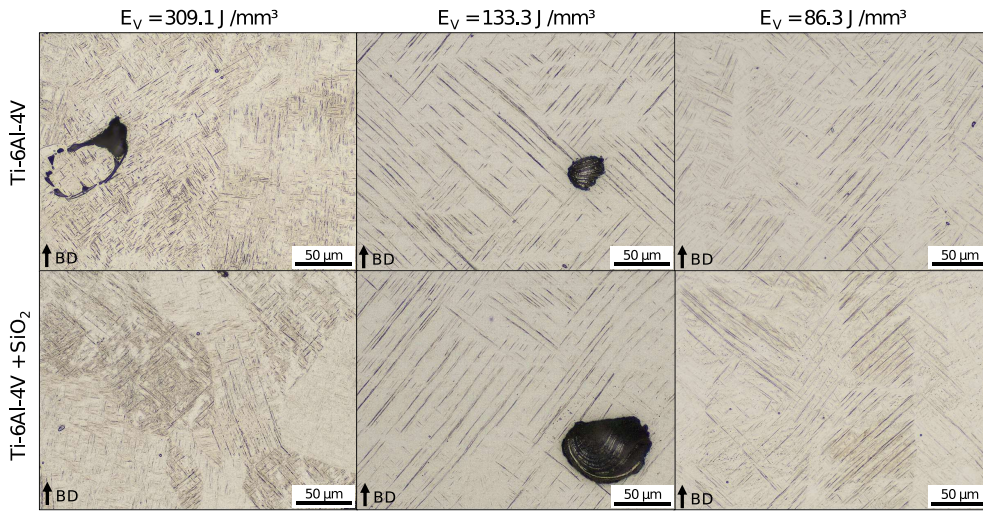


Fig. 9 Cross-section of specimens etched with Kroll's reagent showing the typical fine martensitic microstructure; build direction (BD) is indicated by an arrow; center point parameter setting.

applied method to generate SiO₂ nanoparticles was meant to simulate the SiO₂ generation in a PBF-LB process under silane-induced XHV-adequate atmosphere. In order to give an indication of the amount of SiO₂ produced, Eq. 5 was used, which is based on the calculations by Holländer et al. [6]. Holländer et al. calculated the mass flow of formed SiO₂ due to a constant value of residual oxygen in an open system. In the present case, the flooded machine represents a closed system with a defined initial amount of residual oxygen. The calculation is therefore reduced to the formed mass of SiO₂ m_{SiO_2} in dependence of the regarded gas volume V_{gas} , the contained oxygen x_{O_2} and moisture amount $x_{\text{H}_2\text{O}}$ in this volume under the prerequisite of a temperature of 20 °C and an ambient pressure of 1013 mbar.

$$\frac{m_{\text{SiO}_2}}{g} = 2.5 \cdot 10^{-6} \cdot \frac{V_{\text{gas}}}{l} \cdot \left(\frac{x_{\text{O}_2}}{\text{ppm}} + \frac{1}{2} \frac{x_{\text{H}_2\text{O}}}{\text{ppm}} \right) \quad (5)$$

The generated SiO₂ mass in dependence of different residual oxygen contents was plotted against the regarded machine volume (Fig. 11). Residual moisture was neglected for this calculation. The volume of 30 l of the test chamber described in this work is marked by a vertical line. The machine, in which the XHV-adequate atmosphere will be generated, will be flooded with argon first to already reduce the residual oxygen content as much as possible. Therefore, the plot only displays residual oxygen contents that are realistic for PBF-LB machines. The SiO₂ mass increases linearly with increasing residual oxygen content and increasing flooded machine volume. The greatest possible reduction in the residual oxygen before the addition of silane is therefore essential in order

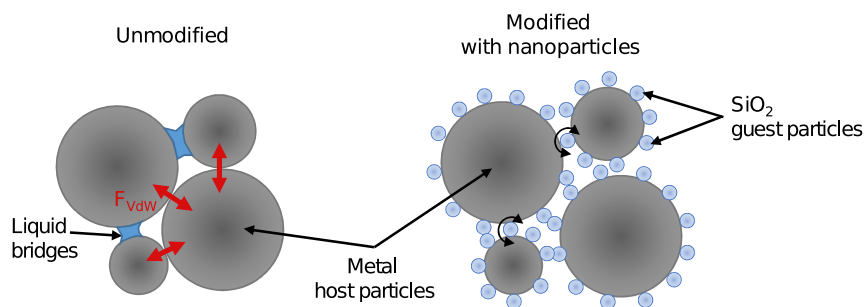


Fig. 10 Interparticulate mechanisms with liquid bridges and Van-der-Waals forces (F_{vdw}) impeding flow of unmodified powders and SiO₂ nanoparticles acting as ball bearings and flow promoters in modified powder.

to keep the generation of dust in the system to a minimum. In this work, the silane content of 1 vol-% was the limiting factor instead of the residual oxygen content, because no prior flooding with argon took place. It becomes clear that this is a very conservative approach and that significantly less SiO₂ will be produced in the real process. Nevertheless, the formed SiO₂ could accumulate in the powder when it is reused multiple times.

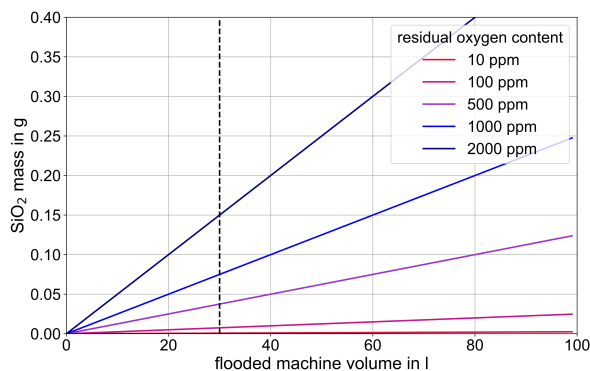


Fig. 11 Formed SiO₂ mass as a function of the flooded machine volume and the residual oxygen (20 °C, 1013 mbar, residual moisture neglected). The vertical line indicates the test chamber volume of 30 l that was considered in this work.

In the future, on the one hand, different concentrations should be tested in order to be able to make quantitative statements about the influence of the nanoparticles. The powder should be investigated after different amount of reusing cycles. In addition, it is expected that the dust could not only have an effect in the powder but also in the atmosphere before it settles. Here the laser radiation can be scattered and thus the energy input can be weakened. This in turn could affect the process window. It is therefore essential to carry out experiments in an XHV-adequate atmosphere, which is now planned as part of the ongoing collaborative research center. An innovative system has already been built for this purpose

[4]. For the specific application of the PBF-LB process in a silane-induced XHV-adequate atmosphere, the described results mean that the expected formation of SiO₂ nanoparticles and their infiltration of the powder is likely to not affect the processing window. In a more general view, the findings indicate that by modifying powders with SiO₂ nanoparticles their flowability can be improved while maintaining the established parameter settings. Consequently, it is possible to process a wider range of powder materials and achieve a broader spectrum of properties for additively manufactured parts.

5 Conclusion

In this work, the influence of SiO₂ nanoparticle modification of Ti-6Al-4V powder on the powder flowability and the PBF-LB process was investigated. The following conclusions can be drawn:

- Powder modification with SiO₂ nanoparticles led to an improvement in flowability, characterized by a reduced flow rate (from 33.3 to 32.5 s/50 g) and an increased apparent density (from 2.52 to 2.58 g/cm³).
- Powder modification had no significant effect on top and side surface roughness, porosity, hardness or microstructure.
- Roughness and porosity were mostly influenced by laser power and scanning speed while scanning speed and hatch distance had the strongest effects on hardness.
- All regression models showed a significant influence of the two-way interaction of laser power and scanning speed, which can be explained by the resulting volume energy density.
- Powder modification with SiO₂ nanoparticles is an effective measure to increase flowability and therefore achieve a wider range of processable powder materials while maintaining the processing window.

Future research will include tensile tests as well as experiments under silane-induced XHV-adequate atmosphere.

Declarations

Acknowledgements

Funded by the Deutsche Forschungsgemeinschaft (DFG, German Research Foundation) – Project-ID 394563137 – SFB 1368.

Conflicts of interest

The authors declare that they have no conflict of interest.

Availability of data and material

The data is stored in the CKAN repository of the SFB 1368 and is available upon request.

Code availability

Not applicable.

Authors' contributions

Nicole Emminghaus: conception; execute trials; analysis; interpretation; visualization; writing - original draft preparation
Robert Bernhard: writing - review and editing; supervision
Jörg Hermsdorf: writing - review and editing; supervision
Stefan Kaieler: writing - review and editing; supervision

References

- Schaper F, Denkena B, Dittrich MA, Krödel A, Matthies J, Worpenberg S (2021) Wear Behaviour of PCBN, PCD, Binderless PCBN and Cemented Carbide Cutting Inserts When Machining Ti-6Al-4V in an Oxygen-Free Atmosphere. In: Behrens BA, Brosius A, Hintze W, Ihlenfeldt S, Wulfsberg JP (eds) *Production at the leading edge of technology*, Springer, Berlin, Heidelberg, pp 275–283, DOI 10.1007/978-3-662-62138-7_28
- Rodriguez Diaz M, Nicolaus M, Möhwald K, Maier HJ (2021) Thermal spraying in silane-doped shielding gases: A new approach for innovative coatings in controlled process atmospheres. *Thermal Spray Bulletin* 14:120–127
- Maier HJ, Herbst S, Denkena B, Dittrich MA, Schaper F, Worpenberg S, Gustus R, Maus-Friedrichs W (2020) Towards Dry Machining of Titanium-Based Alloys: A New Approach Using an Oxygen-Free Environment. *Metals* 10(9):1161, DOI 10.3390/met10091161
- Emminghaus N, Fritsch S, Büttner H, August J, Tegtmeyer M, Huse M, Lammers M, Hoff C, Hermsdorf J, Kaieler S (2021) PBF-LB/M process under a silane-doped argon atmosphere: Preliminary studies and development of an innovative machine concept. *Advances in Industrial and Manufacturing Engineering* 2:100040, DOI 10.1016/j.aime.2021.100040
- Tamanini F, Chaffee JL, Jambor RL (1998) Reactivity and ignition characteristics of silane/air mixtures. *Process Safety Progress* 17(4):243–258, DOI 10.1002/prs.680170405
- Holländer U, Wulff D, Langohr A, Möhwald K, Maier HJ (2020) Brazing in SiH₄-Doped Inert Gases: A New Approach to an Environment Friendly Production Process. *International Journal of Precision Engineering and Manufacturing-Green Technology* 7(6):1059–1071, DOI 10.1007/s40684-019-00109-1
- Redhead PA (1999) Extreme high vacuum. CERN
- Dzogbewu TC (2020) Laser powder bed fusion of Ti6Al4V lattice structures and their applications. *Journal of Metals, Materials and Minerals* 30(4):68–78
- Vignesh M, Ranjith Kumar G, Sathishkumar M, Manikandan M, Rajyalakshmi G, Ramanujam R, Arivazhagan N (2021) Development of Biomedical Implants through Additive Manufacturing: A Review. *Journal of Materials Engineering and Performance* 30(7):4735–4744, DOI 10.1007/s11665-021-05578-7
- Blakey-Milner B, Gradl P, Snedden G, Brooks M, Pitot J, Lopez E, Leary M, Berto F, du Plessis A (2021) Metal additive manufacturing in aerospace: A review. *Materials & Design* 209:110008, DOI 10.1016/j.matdes.2021.110008
- Cepeda-Jiménez CM, Potenza F, Magalini E, Luchin V, Molinari A, Pérez-Prado MT (2020) Effect of energy density on the microstructure and texture evolution of Ti-6Al-4V manufactured by laser powder bed fusion. *Materials Characterization* 163:110238, DOI 10.1016/j.matchar.2020.110238
- Gordon JV, Narra SP, Cunningham RW, Liu H, Chen H, Suter RM, Beuth JL, Rollett AD (2020) Defect structure process maps for laser powder bed fusion additive manufacturing. *Additive Manufacturing* 36:101552, DOI 10.1016/j.addma.2020.101552
- Shipley H, McDonnell D, Culleton M, Coull R, Lupoi R, O'Donnell G, Trimble D (2018) Optimisation of process parameters to address fundamental challenges during selective laser melting of Ti-6Al-4V: A review. *International Journal of Machine Tools and Manufacture* 128:1–20, DOI 10.1016/j.ijmactools.2018.01.003
- Khorasani AM, Gibson I, Ghasemi A, Ghaderi A (2019) A comprehensive study on variability of relative density in selective laser melting of Ti-6Al-4V. *Virtual and Physical Prototyping* 14(4):349–359, DOI 10.1080/17452759.

- 2019.1614198
15. Li Z, Kucukkoc I, Zhang DZ, Liu F (2018) Optimising the process parameters of selective laser melting for the fabrication of Ti6Al4V alloy. *Rapid Prototyping Journal* 24(1):150–159, DOI 10.1108/RPJ-03-2016-0045
 16. Dietrich K, Diller J, Dubiez-Le Goff S, Bauer D, Forêt P, Witt G (2020) The influence of oxygen on the chemical composition and mechanical properties of Ti-6Al-4V during laser powder bed fusion (L-PBF). *Additive Manufacturing* 32:100980, DOI 10.1016/j.addma.2019.100980
 17. Vrancken B, Buls S, Kruth JP, Van Humbeeck J (2015) Influence of preheating and oxygen content on selective laser melting of Ti6Al4V. In: *Proceedings of the 16th RAPDASA Conference*
 18. Velasco-Castro M, Hernández-Nava E, Figueroa IA, Todd I, Goodall R (2019) The effect of oxygen pickup during selective laser melting on the microstructure and mechanical properties of Ti-6Al-4V lattices. *Heliyon* 5(12):e02813, DOI 10.1016/j.heliyon.2019.e02813
 19. Barthel H, Rösch L, Weis J (2005) Fumed silica-production, properties, and applications. *Organosilicon Chemistry Set: From Molecules to Materials* pp 761–778
 20. Berretta S, Ghita O, Evans KE (2014) Morphology of polymeric powders in Laser Sintering (LS): From Polyamide to new PEEK powders. *European Polymer Journal* 59:218–229, DOI 10.1016/j.eurpolymj.2014.08.004
 21. Blümel C, Sachs M, Laumer T, Winzer B, Schmidt J, Schmidt M, Peukert W, Wirth KE (2015) Increasing flowability and bulk density of PE-HD powders by a dry particle coating process and impact on LBM processes. *Rapid Prototyping Journal* 21(6):697–704, DOI 10.1108/RPJ-07-2013-0074
 22. Melnichuk M, Cuscueta DJ, Silin N (2018) Effect of glidants on LaNi5 powder flowability. *International Journal of Hydrogen Energy* 43(12):6219–6228, DOI 10.1016/j.ijhydene.2018.01.207
 23. Karg MC, Rasch M, Schmidt K, Spitzer SA, Karsten TF, Schlaug D, Biaciu CR, Gorunov AI, Schmidt M (2018) Laser alloying advantages by dry coating metallic powder mixtures with siox nanoparticles. *Nanomaterials* 8(10):862
 24. Karg MCH, Munk A, Ahuja B, Backer MV, Schmitt JP, Stengel C, Kuryntsev SV, Schmidt M (2019) Expanding particle size distribution and morphology of aluminium-silicon powders for Laser Beam Melting by dry coating with silica nanoparticles. *Journal of Materials Processing Technology* 264:155–171, DOI 10.1016/j.jmatprotec.2018.08.045
 25. Peng W, Wang G, Gigliotti Jr MFX, Singh P (2018) Method for treating powder by dry mixing and powder treated thereby. US Patent 9,994,716
 26. Gärtner E, Jung HY, Peter NJ, Dehm G, Jäggle EA, Uhlenwinkel V, Mädler L (2021) Reducing cohesion of metal powders for additive manufacturing by nanoparticle dry-coating. *Powder Technology* 379:585–595, DOI 10.1016/j.powtec.2020.10.065
 27. Santeccchia E, Spigarelli S, Cabibbo M (2020) Material Reuse in Laser Powder Bed Fusion: Side Effects of the Laser—Metal Powder Interaction. *Metals* 10(3):341, DOI 10.3390/met10030341
 28. Whip B, Sheridan L, Gockel J (2019) The effect of primary processing parameters on surface roughness in laser powder bed additive manufacturing. *The International Journal of Advanced Manufacturing Technology* 103(9):4411–4422, DOI 10.1007/s00170-019-03716-z
 29. Sharma R, Setia G (2019) Mechanical dry particle coating on cohesive pharmaceutical powders for improving flowability - A review. *Powder Technology* 356:458–479, DOI 10.1016/j.powtec.2019.08.009
 30. Yang J, Sliva A, Banerjee A, Dave RN, Pfeffer R (2005) Dry particle coating for improving the flowability of cohesive powders. *Powder Technology* 158(1):21–33, DOI 10.1016/j.powtec.2005.04.032
 31. Huang Q, Zhang H, Zhu J (2010) Flow properties of fine powders in powder coating. *Particuology* 8(1):19–27, DOI 10.1016/j.partic.2009.05.007
 32. Han M, Zhou Y, Zhu J (2020) Improvement on flowability and fluidization of Group C particles after nanoparticle modification. *Powder Technology* 365:208–214, DOI 10.1016/j.powtec.2019.07.026
 33. Xu CC, Zhang H, Zhu J (2009) Improving flowability of cohesive particles by partial coating on the surfaces. *The Canadian Journal of Chemical Engineering* 87(3):403–414, DOI 10.1002/cjce.20179
 34. Jadhav SD, Dadbakhsh S, Vleugels J, Hofkens J, Van Puyvelde P, Yang S, Kruth JP, Van Humbeeck J, Vanmeensel K (2019) Influence of Carbon Nanoparticle Addition (and Impurities) on Selective Laser Melting of Pure Copper. *Materials* 12(15):2469, DOI 10.3390/ma12152469
 35. Pannitz O, Großwendt F, Lüddecke A, Kwade A, Röttger A, Sehrt JT (2021) Improved Process Efficiency in Laser-Based Powder Bed Fusion of Nanoparticle Coated Maraging Tool Steel Powder. *Materials* 14(13):3465, DOI 10.3390/ma14133465
 36. Sehrt JT, Kleszczynski S, Notthoff C (2017) Nanoparticle improved metal materials for additive manufacturing. *Progress in Additive Manufacturing* 2(4):179–191, DOI 10.1007/s40964-017-0028-9
 37. Simchi A (2006) Direct laser sintering of metal powders: Mechanism, kinetics and microstructural features. *Materials Science and Engineering: A* 428(1):148–158, DOI 10.1016/j.msea.2006.04.117

38. Casalino G, Campanelli SL, Contuzzi N, Ludovico AD (2015) Experimental investigation and statistical optimisation of the selective laser melting process of a maraging steel. *Optics & Laser Technology* 65:151–158, DOI 10.1016/j.optlastec.2014.07.021
39. Wang D, Liu Y, Yang Y, Xiao D (2016) Theoretical and experimental study on surface roughness of 316L stainless steel metal parts obtained through selective laser melting. *Rapid Prototyping Journal* 22(4):706–716, DOI 10.1108/RPJ-06-2015-0078
40. Spierings A, Herres N, Levy G (2011) Influence of the particle size distribution on surface quality and mechanical properties in AM steel parts. *Rapid Prototyping Journal* 17(3):195–202, DOI 10.1108/13552541111124770
41. Yang T, Liu T, Liao W, MacDonald E, Wei H, Chen X, Jiang L (2019) The influence of process parameters on vertical surface roughness of the AlSi10Mg parts fabricated by selective laser melting. *Journal of Materials Processing Technology* 266:26–36, DOI 10.1016/j.jmatprotec.2018.10.015
42. Pal S, Lojen G, Hudak R, Rajtukova V, Brajlilj T, Kokol V, Drstvenšek I (2020) As-fabricated surface morphologies of Ti-6Al-4V samples fabricated by different laser processing parameters in selective laser melting. *Additive Manufacturing* 33:101147, DOI 10.1016/j.addma.2020.101147
43. Khorasani M, Ghasemi A, Awan US, Hadavi E, Leary M, Brandt M, Littlefair G, O’Neil W, Gibson I (2020) A study on surface morphology and tension in laser powder bed fusion of Ti-6Al-4V. *The International Journal of Advanced Manufacturing Technology* 111(9):2891–2909, DOI 10.1007/s00170-020-06221-w
44. Dilip JJS, Zhang S, Teng C, Zeng K, Robinson C, Pal D, Stucker B (2017) Influence of processing parameters on the evolution of melt pool, porosity, and microstructures in Ti-6Al-4V alloy parts fabricated by selective laser melting. *Progress in Additive Manufacturing* 2(3):157–167, DOI 10.1007/s40964-017-0030-2
45. Yang J, Han J, Yu H, Yin J, Gao M, Wang Z, Zeng X (2016) Role of molten pool mode on formability, microstructure and mechanical properties of selective laser melted Ti-6Al-4V alloy. *Materials & Design* 110:558–570, DOI 10.1016/j.matdes.2016.08.036
46. Verhaeghe F, Craeghs T, Heulens J, Pandelaers L (2009) A pragmatic model for selective laser melting with evaporation. *Acta Materialia* 57(20):6006–6012, DOI 10.1016/j.actamat.2009.08.027
47. Cui X, Zhang S, Zhang CH, Chen J, Zhang JB, Dong SY (2021) Additive manufacturing of 24CrNiMo low alloy steel by selective laser melting: Influence of volumetric energy density on densification, microstructure and hardness. *Materials Science and Engineering: A* 809:140957, DOI 10.1016/j.msea.2021.140957
48. Gong H, Rafi K, Gu H, Janaki Ram GD, Starr T, Stucker B (2015) Influence of defects on mechanical properties of Ti-6Al-4V components produced by selective laser melting and electron beam melting. *Materials & Design* 86:545–554, DOI 10.1016/j.matdes.2015.07.147
49. Bartolomeu F, Faria S, Carvalho O, Pinto E, Alves N, Silva FS, Miranda G (2016) Predictive models for physical and mechanical properties of Ti6Al4V produced by Selective Laser Melting. *Materials Science and Engineering: A* 663:181–192, DOI 10.1016/j.msea.2016.03.113
50. Javidrad HR, Ghanbari M, Javidrad F (2021) Effect of scanning pattern and volumetric energy density on the properties of selective laser melting Ti-6Al-4V specimens. *Journal of Materials Research and Technology* 12:989–998, DOI 10.1016/j.jmrt.2021.03.044
51. Ladewig A, Schlick G, Fisser M, Schulze V, Glatzel U (2016) Influence of the shielding gas flow on the removal of process by-products in the selective laser melting process. *Additive Manufacturing* 10:1–9, DOI 10.1016/j.addma.2016.01.004
52. Parteli EJR, Pöschel T (2016) Particle-based simulation of powder application in additive manufacturing. *Powder Technology* 288:96–102, DOI 10.1016/j.powtec.2015.10.035
53. Metel AS, Stebulyanin MM, Fedorov SV, Okunkova AA (2019) Power Density Distribution for Laser Additive Manufacturing (SLM): Potential, Fundamentals and Advanced Applications. *Technologies* 7(1):5, DOI 10.3390/technologies7010005
54. Strondl A, Lyckfeldt O, Brodin H, Ackelid U (2015) Characterization and Control of Powder Properties for Additive Manufacturing. *JOM* 67(3):549–554, DOI 10.1007/s11837-015-1304-0
55. Sutton AT, Kriewall CS, Karnati S, Leu MC, Newkirk JW (2020) Characterization of AISI 304L stainless steel powder recycled in the laser powder-bed fusion process. *Additive Manufacturing* 32:100981, DOI 10.1016/j.addma.2019.100981
56. Li C, Sun S, Zhang Y, Liu C, Deng P, Zeng M, Wang F, Ma P, Li W, Wang Y (2019) Effects of laser processing parameters on microstructure and mechanical properties of additively manufactured AlSi10Mg alloys reinforced by TiC. *The International Journal of Advanced Manufacturing Technology* 103(5):3235–3246, DOI 10.1007/s00170-019-04001-9
57. Gu D, Wang H, Chang F, Dai D, Yuan P, Hagedorn YC, Meiners W (2014) Selective Laser Melting Additive Manufacturing of TiC/AlSi10Mg Bulk-form Nanocomposites with Tailored Microstructures and Properties. *Physics Procedia* 56:108–116, DOI 10.1016/j.phpro.2014.08.153
58. Gu D, Wang H, Dai D, Chang F, Meiners W, Hagedorn YC, Wissenbach K, Kelbassa I, Poprawe R (2015) Den-

sification behavior, microstructure evolution, and wear property of tic nanoparticle reinforced alsil0mg bulk-form nanocomposites prepared by selective laser melting. Journal of Laser Applications 27(S1):S17003

59. Zhu J, Kamiya A, Yamada T, Watazu A, Shi W, Naganuma K (2001) Effect of Silicon Addition on Microstructure and Mechanical Properties of Cast Titanium Alloys. Materials Transactions 42(2):336–341, DOI 10.2320/matertrans.42.336
60. Deng T, Li S, Liang Y, Sun L, Zhang Y (2020) Effects of scandium and silicon addition on the microstructure and mechanical properties of Ti-6Al-4V alloy. Journal of Materials Research and Technology 9(3):5676–5688, DOI 10.1016/j.jmrt.2020.03.092
61. Lütjering G, Williams JC (2007) High Temperature Alloys. In: Lütjering G, Williams JC (eds) Titanium, Springer, Berlin, Heidelberg, pp 259–282, DOI 10.1007/978-3-540-73036-1_6
62. Morgan AE, Broadbent EK, Ritz K, Sadana D, Burrow B (1988) Interactions of thin ti films with si, sio2, si3n4, and sio x n y under rapid thermal annealing. Journal of applied physics 64(1):344–353

Prediction expression for hardness H

$$\begin{aligned} \frac{H}{HV0.1} = & 414.0361 + 5.0632 \cdot \left(\frac{P-145W}{15W} \right) - 8.3912 \cdot \left(\frac{v-700 \frac{mm}{s}}{300 \frac{mm}{s}} \right) \\ & - 8.2953 \cdot \left(\frac{h-80\mu m}{20\mu m} \right) - 5.1552 \cdot \left(\frac{P-145W}{15W} \right)^2 \\ & + 5.3438 \cdot \left(\left(\frac{P-145W}{15W} \right) \cdot \left(\frac{v-700 \frac{mm}{s}}{300 \frac{mm}{s}} \right) \right) - 4.6102 \cdot \left(\frac{v-700 \frac{mm}{s}}{300 \frac{mm}{s}} \right)^2 \end{aligned} \quad (a4)$$

Appendix

Prediction expression for top surface roughness S_{aTop}

$$\begin{aligned} \frac{S_{aTop}}{\mu m} = & \exp \left(2.5741 - 0.1561 \cdot \left(\frac{P-145W}{15W} \right) + 0.3510 \cdot \left(\frac{v-700 \frac{mm}{s}}{300 \frac{mm}{s}} \right) \right. \\ & - 0.1601 \cdot \left(\left(\frac{P-145W}{15W} \right) \cdot \left(\frac{v-700 \frac{mm}{s}}{300 \frac{mm}{s}} \right) \right) + 0.0097 \cdot \left(\frac{v-700 \frac{mm}{s}}{300 \frac{mm}{s}} \right)^2 \\ & \left. - 0.1127 \cdot \left(\frac{v-700 \frac{mm}{s}}{300 \frac{mm}{s}} \right)^3 \right) \end{aligned} \quad (a1)$$

Prediction expression for side surface roughness S_{aSide}

$$\begin{aligned} \frac{S_{aSide}}{\mu m} = & \exp \left(2.2950 - 0.0025 \cdot \left(\frac{P-145W}{15W} \right) + 0.0369 \cdot \left(\frac{v-700 \frac{mm}{s}}{300 \frac{mm}{s}} \right) \right. \\ & - 0.0890 \cdot \left(\left(\frac{P-145W}{15W} \right) \cdot \left(\frac{v-700 \frac{mm}{s}}{300 \frac{mm}{s}} \right) \right) + 0.0820 \cdot \left(\frac{P-145W}{15W} \right)^2 \\ & \left. + 0.1623 \cdot \left(\frac{v-700 \frac{mm}{s}}{300 \frac{mm}{s}} \right)^2 - 0.0801 \cdot \left(\frac{v-700 \frac{mm}{s}}{300 \frac{mm}{s}} \right)^3 \right) \end{aligned} \quad (a2)$$

Prediction expression for porosity ϕ

$$\begin{aligned} \frac{\phi}{\%} = & \exp \left(-1.8816 - 0.5779 \cdot \left(\frac{P-145W}{15W} \right) - 0.0849 \cdot \left(\frac{v-700 \frac{mm}{s}}{300 \frac{mm}{s}} \right) \right. \\ & + 0.2867 \cdot \left(\frac{h-80\mu m}{20\mu m} \right) - 0.5827 \cdot \left(\left(\frac{P-145W}{15W} \right) \cdot \left(\frac{v-700 \frac{mm}{s}}{300 \frac{mm}{s}} \right) \right) \\ & + 0.2649 \cdot \left(\left(\frac{P-145W}{15W} \right) \cdot \left(\frac{h-80\mu m}{20\mu m} \right) \right) \\ & + 0.4149 \cdot \left(\frac{v-700 \frac{mm}{s}}{300 \frac{mm}{s}} \right) \cdot \left(\frac{h-80\mu m}{20\mu m} \right) + 0.3276 \cdot \left(\frac{P-145W}{15W} \right)^2 \\ & \left. + 0.7526 \cdot \left(\frac{v-700 \frac{mm}{s}}{300 \frac{mm}{s}} \right)^2 \right) \end{aligned} \quad (a3)$$

Table A1 Specimen IDs with corresponding parameter settings.

Specimen ID	Laser power (W)	Scanning speed (mm/s)	Hatch distance (μm)
1	145.0	700.0	80.0
2	170.2	700.0	80.0
3	145.0	1204.5	80.0
4	145.0	195.5	80.0
5	160.0	400.0	100.0
6	145.0	700.0	80.0
7	145.0	700.0	80.0
8	130.0	1000.0	60.0
9	145.0	700.0	80.0
10	160.0	1000.0	100.0
11	130.0	1000.0	100.0
12	130.0	1000.0	100.0
13	130.0	400.0	60
14	145.0	700.0	113.6
15	170.2	700.0	80.0
16	145.0	700.0	80.0
17	145.0	700.0	113.6
18	160.0	1000.0	60.0
19	130.0	1000.0	60.0
20	160.0	400.0	60.0
21	130.0	400.0	60.0
22	145.0	700.0	46.4
23	130.0	400.0	100.0
24	119.8	700.0	80.0
25	119.8	700.0	80.0
26	160.0	400.0	100.0
27	160.0	1000.0	60.0
28	160.0	400.0	60.0
29	145.0	700.0	46.4
30	160.0	1000.0	100.0
31	145.0	1204.5	80.0
32	145.0	195.5	80.0
33	130.0	400.0	100.0
34	145.0	700.0	80.0

Table A2 Si content in EDX analysis of selected cross-sections.

Specimen ID	Powder	Si content (wt-%)	Minimum detection limit	Si content (at-%)	Error (%)
4	unmodified	0.4	0.08	0.7	11.1
5	unmodified	0.5	0.08	0.7	11
9	unmodified	0.4	0.08	0.7	11.1
11	unmodified	0.5	0.08	0.8	11.1
4	modified	0.5	0.08	0.8	11
5	modified	0.5	0.08	0.8	10.3
9	modified	0.5	0.08	0.8	12.1
11	modified	0.5	0.08	0.8	11.7